Supporting information

for

Demonstrating Electrochemical CO_2 Capture with Redox-Active Metal-Organic Frameworks

Iuliia Vetik,[a] Nikita Žoglo,[b] Akmal Kosimov,[c] Ritums Cepitis,[c]

Veera Krasnenko,[d] Jaan Leis,[a] Maike Käärik,[a] Artis Kons,[e]

Huilin Qing,[f] Priyanshu Chandra,[f] Katherine Mirica,[f]

Ruben Rizo,[c] Enrique Herrero,[c] Jose Solla-Gullón,[c]

Teedhat Trisukhon,[g] Jamie W. Gittins,[g] Alexander C. Forse,[g]

Vitali Grozovski,[a] Nadezda Kongi[a]† and Vladislav Ivaništšev,[e]†

[a] Institute of Chemistry, University of Tartu, Tartu 50411, Estonia

[b] RedoxNRG OÜ, Narva-Jõesuu 29021, Estonia

[c] Institute of Electrochemistry, University of Alicante, Apdo. 99, 03080, Alicante, Spain

[d] Institute of Physics, University of Tartu, Tartu 50411, Estonia

[e] Department of Chemistry, University of Latvia, Riga LV-1004, Latvia

[f] Department of Chemistry, Burke Laboratory, Dartmouth College, New Hampshire 03755, United States

[g] Yusuf Hamied Department of Chemistry, University of Cambridge, Cambridge CB2 1EW, UK

Table S1. Comparison of experimental capacity and adsorption enthalpy values for selected CO_2 sorbents. Theoretical capacity values per molar mass of the sorbent are given in parentheses.

Sorbent material	Capacity [mmol g^{-1}]	Conditions	Adsorption enthalpy [kJ mol^{-1}]	Ref.
Absorption				
Oxide: CaO	17.9	any	−172	1
Monoethanolamine 30 wt%	2.5 (8)	100% CO_2, 1 atm	−82	2
Ionic liquid: [hmim][Tf_2N]	1.2	100% CO_2 13 atm	−13	3
Adsorption				
MOF: SIFSIX-3-Cu	1.2	400 ppm CO_2	−54	4
Zeolite: 13-XPEI	1.2	100% CO_2, 1 atm	−35	5
Electrosorption				
Poly(1,4-anthraquinone)	8.4* (9.7)	CO_2 sat. org. electrolyte	−86	6
MOF: $Cu_3(HHTP)_2$	0.8–2.4* (14.5)	CO_2 sat. aq. electrolyte	−20**	This work

* Estimated from CV data.

** Calculated at the DFT level *via* vibrational analysis.

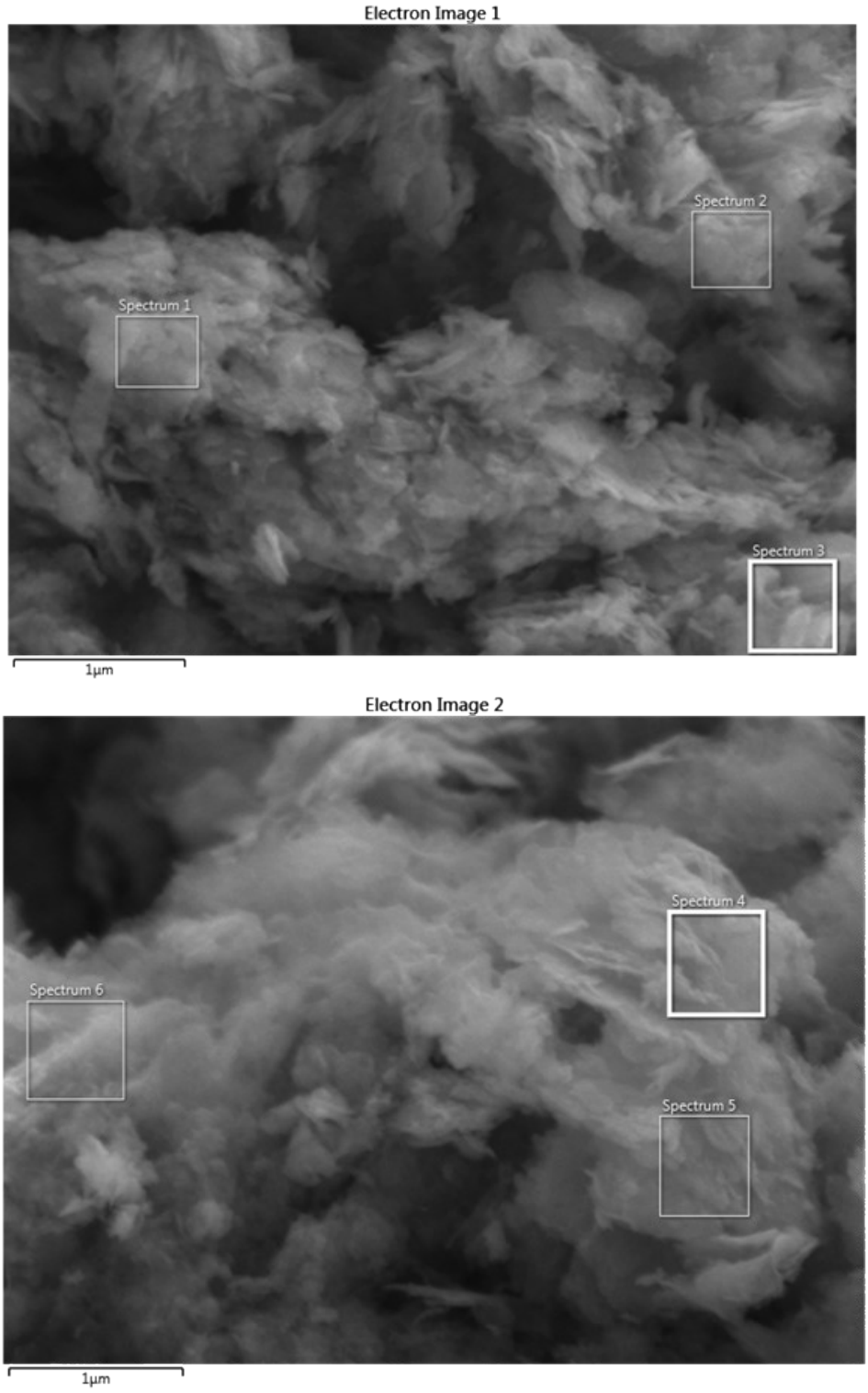

Figure S1. Scanning electron microscope (SEM) images obtained for $Cu_3(HHTP)_2$ during the energy dispersive X-ray (EDX) microanalysis with areas of analysis indicated by squares.

Table S2. The surface elemental composition of the $Cu_3(HHTP)_2$ sample obtained by the energy dispersive X-ray microanalysis. Some nitrogen content arises from the aqueous ammonia used in the synthesis and has been observed previously.[7]

Spectrum	C	O	N	Cu
1	53.4	16.1	2.4	28.1
2	53.7	15.1	2.1	29.2
3	52.1	16.6	2.7	28.6
4	55.5	14.8	1.6	28.2
5	54.4	14.2	1.2	30.2
6	53.5	18.5	2.4	25.6
Average	**53.8**	**15.9**	**2.1**	**28.3**
Error	1.1	1.6	0.6	1.5
Calculated[7]	**52.3**	**23.1**	**0**	**23.1**

Table S3. Elemental analysis for C, H, and N content of the $Cu_3(HHTP)_2$ sample and inductively coupled plasma optical emission spectroscopy (ICP-OES) results for Cu content. Some nitrogen content arises from the aqueous ammonia used in the synthesis and has been observed previously.[7]

Element	Calculated[7] (wt%)	Reference[7] (wt%)	Average found (wt%)
C	52.3	48.9	**41.8**
H	1.5	2.4	**3.3**
N	0	2.8	**4.3**
Cu	23.1	21.7	**18.5**

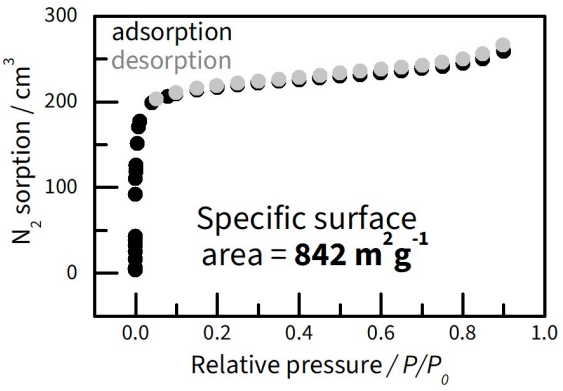

Figure S2. N_2 sorption isotherm for $Cu_3(HHTP)_2$.

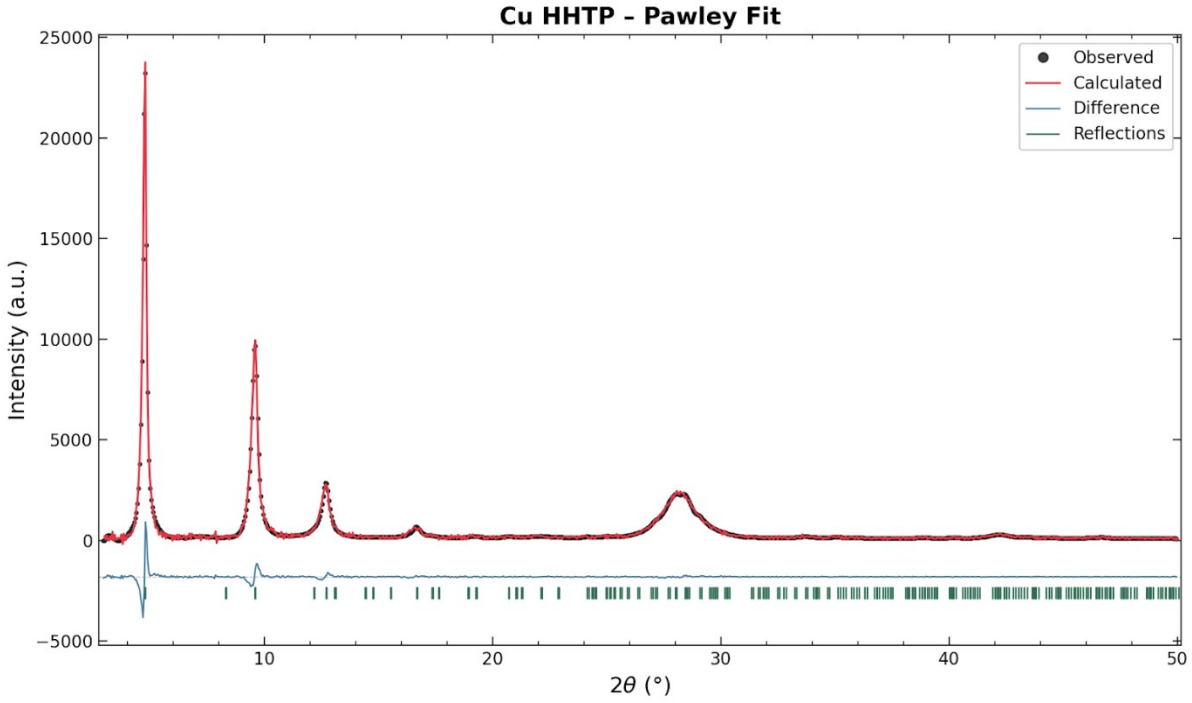

Figure S3. Pawley refinement plot of the XRD data for the sample of $Cu_3(HHTP)_2$.

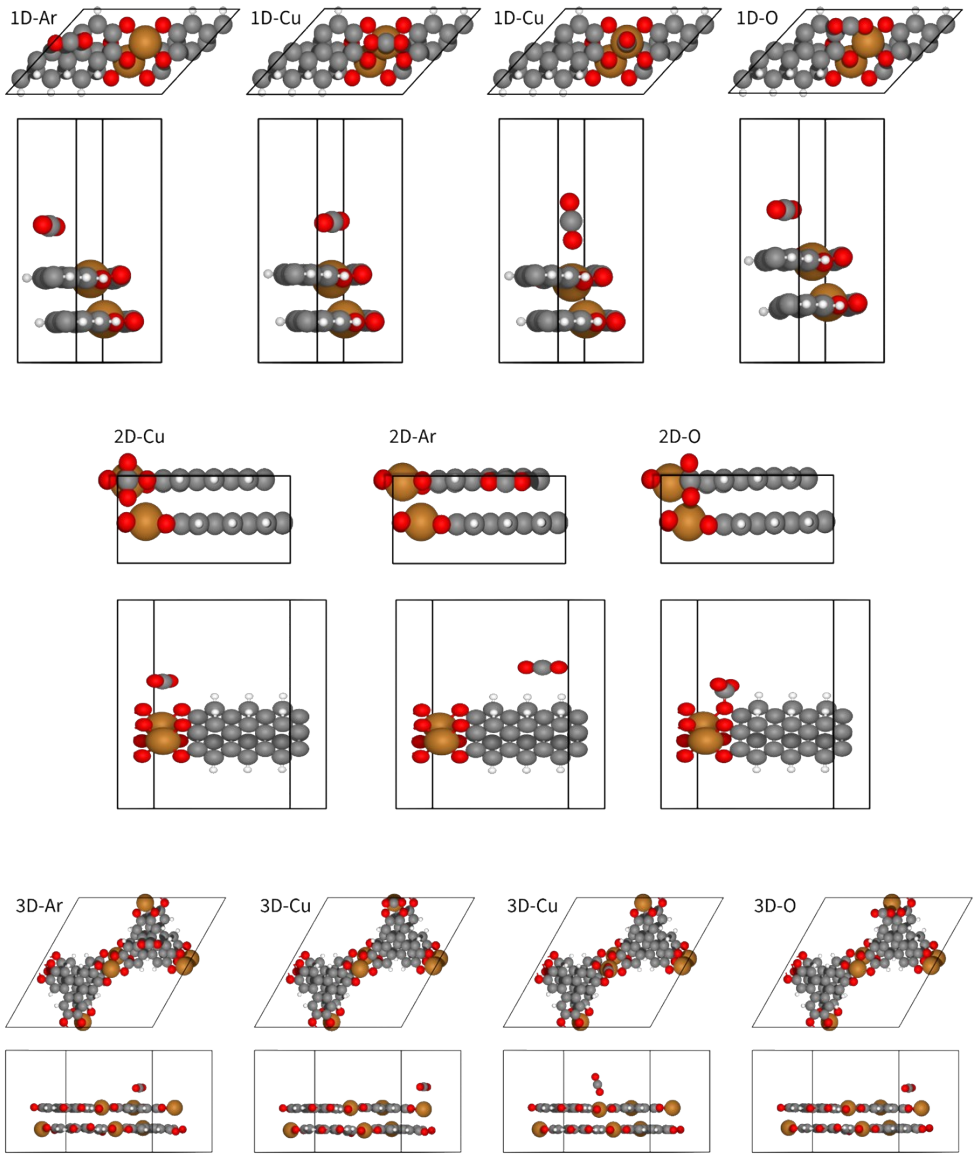

Figure S4. Top and side views on three models (**1D**, **2D**, and **3D**) of Cu-HHTP with the CO_2 molecule adsorbed at three sites (above **Cu**, **O**, **Ar**omatic system) and in two positions (adsorption through C or O in CO_2). The top view is labelled and situated above the side view of each model. The CO_2 molecule is seen in all side views, where the bent geometry of CO_2 indicates chemisorption (in the **2D-O** model). One- and two-dimensional (1D and 2D) models represent in-pore and terminal adsorption sites of a model MOF with features of Cu-HHTP: CuO_4 unit and three aromatic rings. The three-dimensional (3D) model represents terminal adsorption sites of $Cu_3(HHTP)_2$. In each model, there are two layers in the unit cell. For computational details, see the "Density Functional Theory (DFT) calculations" section below. All computational data are available in the format of the Atomic Simulation Environment database from Zenodo at DOI:10.5281/zenodo.14216403.

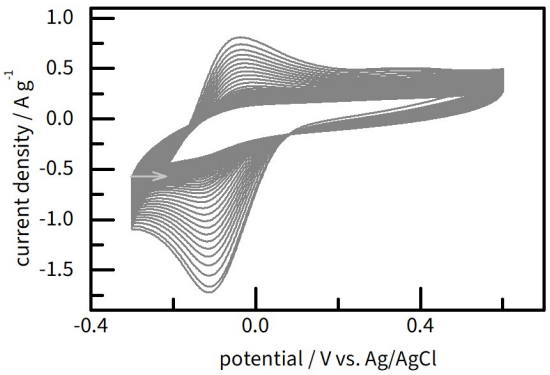

Figure S5. $Cu_3(HHTP)_2$ stabilisation in Ar-saturated 0.1 M $NaClO_4$ electrolyte. Cyclic voltammetry (CV) curves were recorded over 40 cycles for $Cu_3(HHTP)_2$-modified GC electrode at a scan rate of 10 mV s^{-1}.

The observed change in electrochemical behaviour is similar to previously reported dependences of redox activity on thickness,[8] and microstructure of $Cu_3(HHTP)_2$.[9] Zhao et al. showed that with a decrease of $Cu_3(HHTP)_2$ film thickness, the electrochemical behaviour changes from redox-active to capacitive, which is in line with decreasing the charge transfer resistance in impedance spectra.[8] Similarly, Gittins et al. showed that for finer microstructure grinding, the electrochemical behaviour was found to be limited by the ion mass transport resulting in lower current densities.[9] The mass-transport lamination is apparent for $Cu_3(HHTP)_2$ in this work (Fig. S6). Thus, it is possible to interpret the results in Fig. S4 as a structural transformation of $Cu_3(HHTP)_2$.

The disappearance of the cathodic peak at −0.16 V in Fig. S4 is unrelated to oxygen, as it diminishes with time, even in oxidative conditions in electrolytes saturated with air and O_2. The electroreduction of oxygen is expected to happen at lower potentials.[10] The observed change is also unrelated to the reduction of Cu, which potentially could remain from synthesis or form by MOF-s decomposition. Thus, the redox activity of pure MOF in the Ar-saturated 0.1 M $NaClO_4$ electrolyte (as well as in $NaHCO_3$, Na_2SO_4, and NaCl) is probably due to the restructuring, as suggested above.

Redox peaks observed in Fig. S4 were reported in previous works.[11–13] X-ray photoelectron spectroscopy revealed simultaneous reduction of Cu^{2+} to Cu^{+} and quinoid (C=O) to benzenoid (C–O) group.[12,13] XPS analysis of $Cu_3(HHTP)_2$ of variable morphology showed that predominant oxidation state of copper is +2,[14] and charge of −3 on HHTP,[15] due to 1:1 ratio between C–O to C=O. Notably, in 1 M KOH aqueous electrolyte, the discussed reduction is reversible by 99% after 1000 galvanostatic charge and discharge cycles.[16]

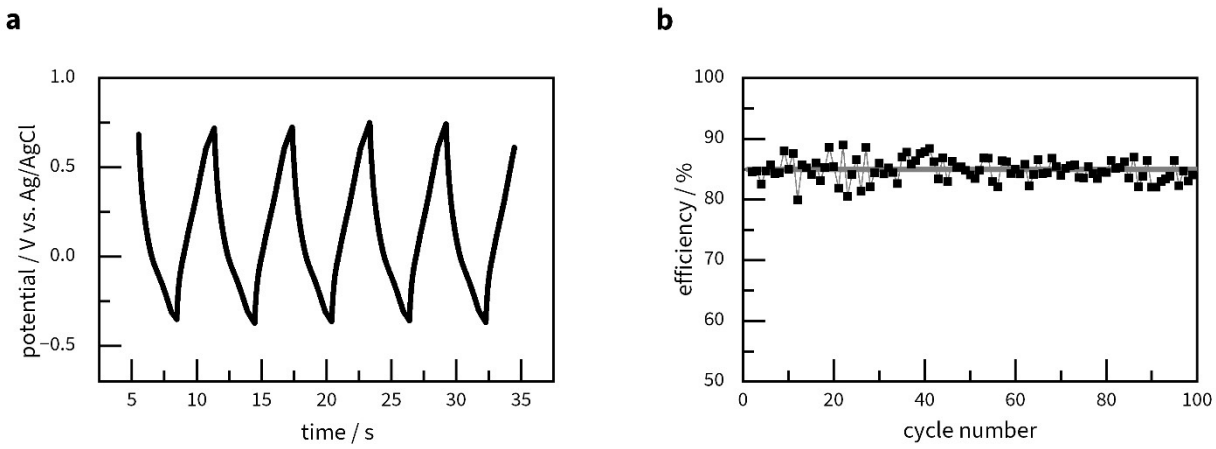

Figure S6. (a) First cycles of the galvanostatic charge/discharge (GCD) experiment for the $Cu_3(HHTP)_2$-modified GC electrode in a CO_2-saturated 0.1 M $NaClO_4$ electrolyte. The mean charge energy, determined by integrating the charge-discharge curves, was $8.5 \cdot 10^{-9}$ W·h, while the discharge energy was $7.2 \cdot 10^{-9}$ W·h. **(b)** The energy efficiency of $Cu_3(HHTP)_2$ calculated over 100 charge-discharge cycles, with the mean value of 85% represented by the grey line.

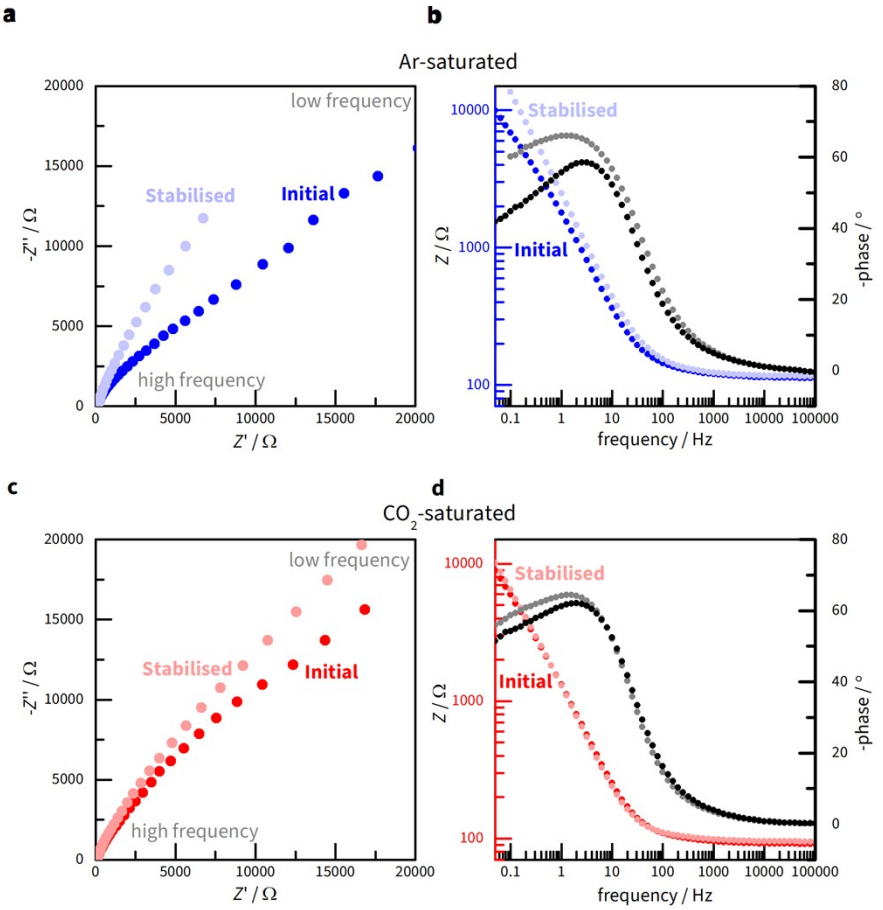

Figure S7. Electrochemical impedance spectroscopy (EIS) experiments performed with a $Cu_3(HHTP)_2$-modified GC electrode in Ar-saturated and CO_2-saturated 0.1 M $NaClO_4$ electrolyte. **(a) and (c)** Nyquist plots and **(b) and (d)** Bode plots. Darker points represent experimental data (blue: Ar-saturated electrolyte; red: CO_2-saturated electrolyte) for unstabilized $Cu_3(HHTP)_2$, while lighter points correspond to stabilized MOF.

At −0.3 V, the impedance data fit well to a model featuring a Warburg element, indicating that mass transport or diffusion-like processes play an important role in the system. The nearly negligible charge-transfer resistance (R_{ct} = 6 μΩ) suggests that electron transfer through the $Cu_3(HHTP)_2$ interface is extremely facile under these conditions, making the primary rate limitation more associated with diffusion of ions or CO_2 within the porous framework. The double-layer capacitance (C_{dl} = 32–68 μF) aligns with typical interfacial values for such conductive MOF-based electrodes, while the Warburg coefficient (Y_0 = 89–180 μMho $s^{0.5}$) captures the characteristic $\omega^{-0.5}$ dependence of diffusion-controlled impedance. Overall, the strong Warburg component suggests that at lower frequencies (down to 0.1 Hz) the system's response is dominated by the transport of adsorbate or ions in the MOF structure rather than by charge-transfer kinetics at the electrode surface.

Table S4. Electrochemical impedance spectroscopy (EIS) fitting results

Potential / V vs. Ag/AgCl	Circuit	Electrolyte resistance / Ω	Capacitance / μF	Y_0 / μMho·$s^{0.5}$	Resistance / μΩ	Capacitance / mF	χ^2
Initial in Ar-saturated electrolyte							
-0.145	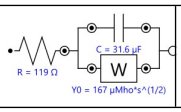	119	32	167	-	-	0.42
Stabilised in Ar-saturated electrolyte							
-0.145	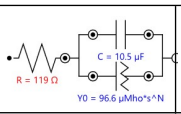	119	11	97 (α = 0.7)	-	-	0.09
-0.145		119	32	89	-	-	0.55
-0.145	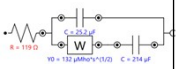	119	25	132		0.2	0.3
-0.145	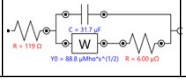	119	32	89	6	-	0.55
Initial in CO_2-saturated electrolyte							
-0.3	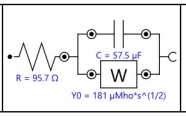	95	58	181	-	-	0.22
Stabilised in CO_2-saturated electrolyte							
-0.3	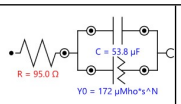	95	54	172 (α = 0.57)	-	-	0.15
-0.3	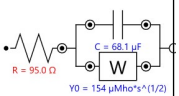	95	68	154	-	-	0.3
-0.3		95	65	166	-	3.6	0.25
-0.3		95	68	154	6	-	0.3

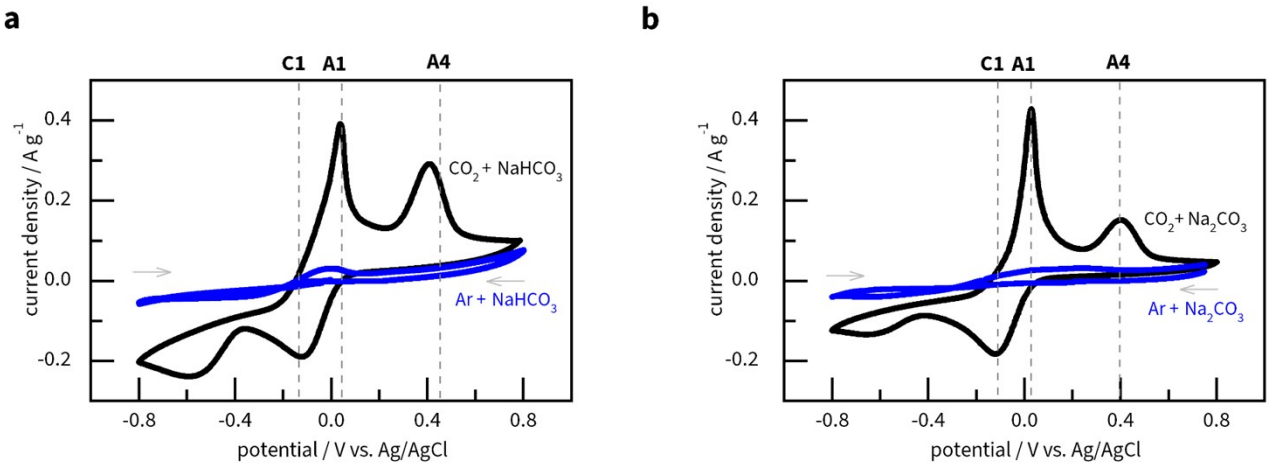

Figure S8. CV curves recorded for $Cu_3(HHTP)_2$-modified GC electrode at ν = 10 mV s^{-1} in 0.1 M $NaClO_4$ electrolyte. **(a)** blue line – Ar-saturated electrolyte with 20 mM of $NaHCO_3$, black – CO_2-saturated electrolyte with 20 mM of $NaHCO_3$; **(b)** blue line – Ar-saturated electrolyte with 20 mM of Na_2CO_3, black – CO_2-saturated electrolyte with 20 mM of Na_2CO_3.

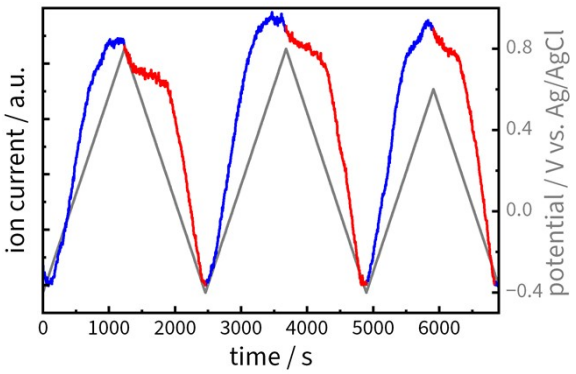

Figure S9. DEMS: ion current of *m/z* = +44 $[CO_2]^+$ during CV at ν = 1 mV s^{-1} for the GC-$Cu_3(HHTP)_2$ working electrode in the presence of CO_2: red line – negative going scan, blue line – positive going scan, with the corresponding working electrode potential (right axis).

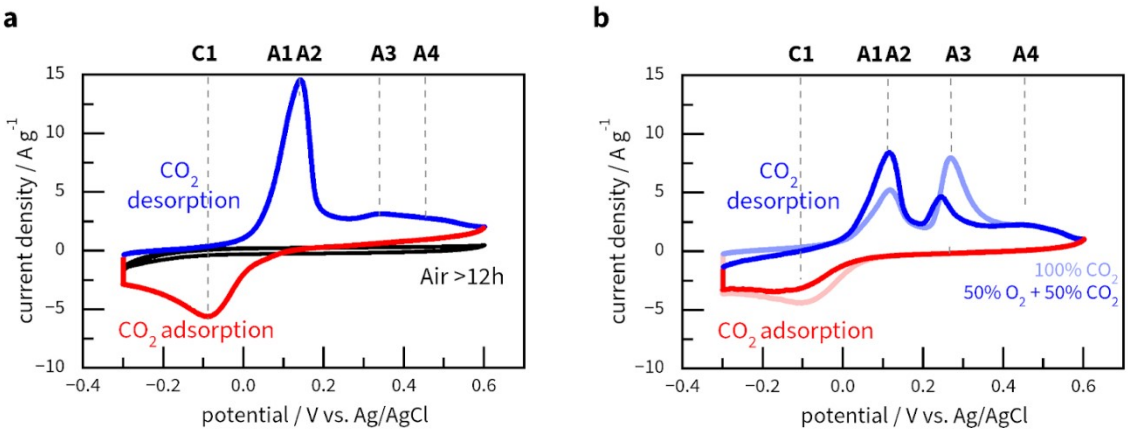

Figure S10. CV curves recorded at v = 10 mV s^{-1} for the $Cu_3(HHTP)_2$-modified GC electrode in 0.1 M $NaClO_4$ electrolyte: **(a)** The curves are measured after 5000 cycles in the air-saturated electrolyte. The black line is recorded in the air-saturated electrolyte, while the red and blue lines correspond to scans in electrolyte re-saturated with CO_2 and after polarization for 10 min at −0.3 V: the red line represents the negative direction, and the blue line represents the positive direction; **(b)** the pale red and pale blue lines correspond to scans in CO_2-saturated electrolyte after polarization for 10 min at −0.3 V. The red and blue lines correspond to scans in (50% CO_2 + 50% O_2)-saturated electrolyte after polarization for 10 min at −0.3 V: the red line represents the negative direction, and dark blue line represents the positive direction.

It is notable that 10 min polarization at −0.3 V is not enough for reaching saturation, i.e. the full sorption capacity, in the (50% CO_2 + 50% O_2)-saturated electrolyte, differently from the CO_2-saturated electrolyte. That is due to lower concentration of CO_2, which is also the reason why the shape of C1 peaks differ for these electrolytes. Insufficient saturation results in higher amplitude of A1/A2 peak for the (50% CO_2 + 50% O_2)-saturated electrolyte similarly to the higher amplitude in Fig. 3 in comparison to Fig. 4. Longer polarization and higher CO_2 concentration are needed for the appearance of A3 and A4 peaks. Still, the amount of desorbed CO_2 is comparable and, thus, it can be concluded that O_2 does not impede the CO_2 electrosorption.

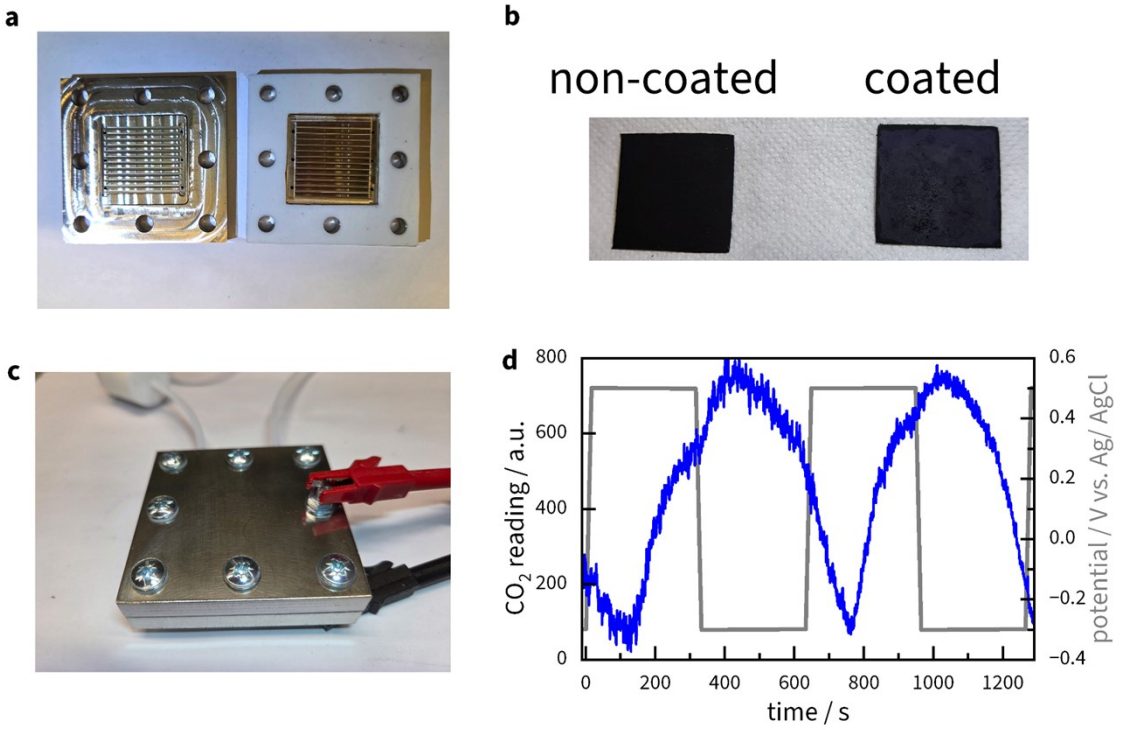

Figure S11: (a) Disassembled electrochemical gas flow cell; **(b)** carbon paper electrode, both uncoated (left) and coated with $Cu_3(HHTP)_2$ (right); **(c)** fully assembled electrochemical gas flow cell; **(d)** CO_2 concentration at the cell outlet (blue line), measured downstream of a carbon paper electrode loaded with 10 mg of $Cu_3(HHTP)_2$, where CO_2 was adsorbed/desorbed upon air introduction at the inlet. The corresponding working electrode potential is shown on the right axis. Duration of 300 seconds per half-cycle was found to be optimal based on the dynamic response of the system. At shorter cycle times, the CO_2 adsorption–desorption transitions would be incomplete, leading to attenuated amplitudes and underestimation of capture–release efficiency. Extending the cycle length to longer times would not further increase uptake/release, indicating that equilibrium was already reached well within 300 s.

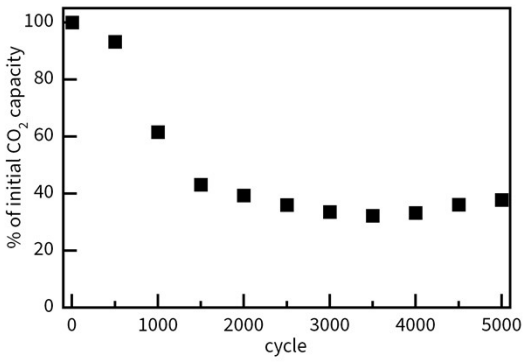

Figure S12. The drop in CO_2 capacity was studied during long-term cycling of the GC-$Cu_3(HHTP)_2$ electrode in a CO_2-saturated 0.1 M $NaClO_4$ electrolyte, within a potential range of −0.3 V to +0.7 V. The capacity reaches a plateau at approximately 30% after 2000 cycles.

After every 100 cycles at a scan rate of 200 mV s^{-1}, the electrode was polarized for 1 minute to ensure CO_2 saturation. CV was then recorded at a scan rate of 10 mV s^{-1}. The CO_2 capacity of the material was determined by integrating the area under the CV curve in the anodic region and subtracting the corresponding area under CV in an Ar atmosphere, using the equation:

$$C = (A_{CO_2} - A_{Ar}) \cdot (v \cdot F)^{-1}$$

where C is the CO_2 capacity of the MOF, A_{CO_2} is the area under the positive-going scan measured in CO_2, A_{Ar} is the area under the positive-going scan measured in Ar, v is the scan rate, and F is the Faraday constant. CO_2 capture was estimated under the assumption that 1 electron induces adsorption-desorption of one CO_2 molecule.

Herewith, the experimentally observed lowering of CO_2 capacity from 2 to 0.8 mmol g^{-1} after 2 hours of cycling could be related to clogging of pores. These numbers indicate a potential for improvement through further optimisation of redox-active MOFs. Namely, adjusting the polarisation times and conditions needed to saturate and desaturate MOFs, i.e., respective CO_2 capture and release.

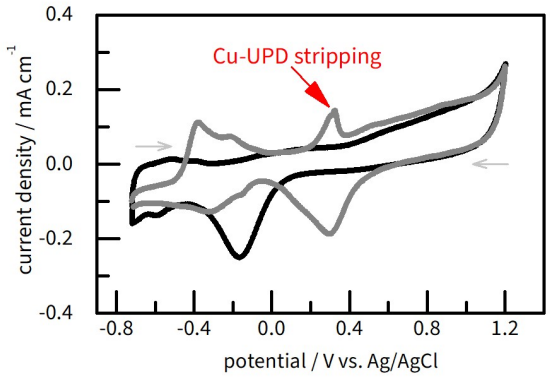

Figure S13. Cyclic voltammetry (CV) curves for copper stripping from Pt electrode, recorded at scan rate of 50 mV s^{-1}, after Cu^{2+} underpotential deposition (UPD) from electrolyte extracted after experiments with $Cu_3(HHTP)_2$. The UPD was run for 20 cycles in the potential window from 0 to −0.72 V. This experiment tests contamination of the electrolyte by Cu^{2+} due to decomposition of $Cu_3(HHTP)_2$ MOF. Grey line – CV curve in the electrolyte obtained after cycling $Cu_3(HHTP)_2$ for 1000 cycles in the potential range of −0.8 V to +0.8 V, anodic peak at 0.35 V on a grey line indicates Cu-UPD stripping.[17] Black line – CV in the electrolyte obtained after cycling $Cu_3(HHTP)_2$ for 5000 cycles in the potential range of −0.3 V to +0.7 V. The absence of the Cu-UPD peak on the black line proves that $Cu_3(HHTP)_2$ does not release Cu^{2+} during operation within the window used to study the CO_2 electrosorption.

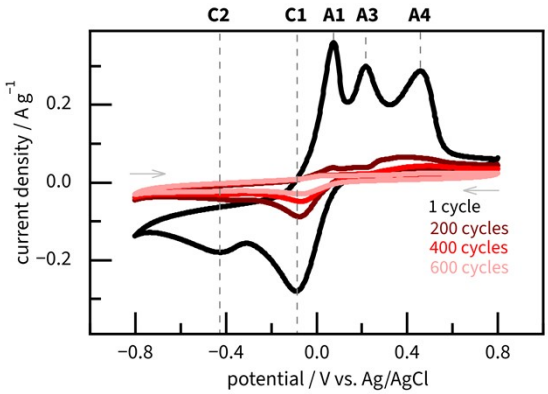

Figure S14. CV curves recorded after long-term cycling at $\Box$ = 10 mV s^{-1} in CO_2-saturated 0.1 M $NaClO_4$ electrolyte for GC-$Cu_3(HHTP)_2$ in the potential range from −0.8 V to +0.8 V: black – after 1 cycle, dark brown – after 200 cycles, red – after 400 cycles, light pink – after 600 cycles. The expected product of decomposition is Cu_2O.[18] Besides, the decomposition releases Cu^{2+} ions to the electrolyte (see Fig. S12).

Synthesis of $Ni_3(HHTP)_2$ and $Co_3(HHTP)_2$

$Ni(OAc)_2 \times 4H_2O$ (0.099 g, 0.4 mmol, 2 eq) and HHTP (0.065 g, 0.2 mmol, 1 eq) were dissolved in H_2O (40 mL). The reaction mixture was sonicated for 20 minutes and then heated at 85 °C for 24 hours. The solid residue was washed with water, ethanol and acetone. The product was activated with ethanol (4×10 mL) and then dried in a vacuum oven at 50 °C overnight. $Ni_3(HHTP)_2$ was obtained as a black solid with a crystalline structure as follows from the powder X-ray diffraction (PXRD) analysis (Fig. S13a).

A similar procedure was used for the synthesis of $Co_3(HHTP)_2$. $Co(OAc)_2 \times 4H_2O$ (0.996 g, 0.4 mmol, 2 eq) and HHTP (0.065 g, 0.2 mmol, 1 eq) were dissolved in H_2O (15 mL) and N-methylpyrrolidone (1.65 mL), the reaction mixture was sonicated for 20 minutes and then heated at 85 °C for 24 hours. The product was activated with ethanol (4×10 mL) and then dried in a vacuum oven at 50 °C overnight. $Co_3(HHTP)_2$ was obtained as a black solid with a crystalline structure as follows from the PXRD analysis (Fig S13b).

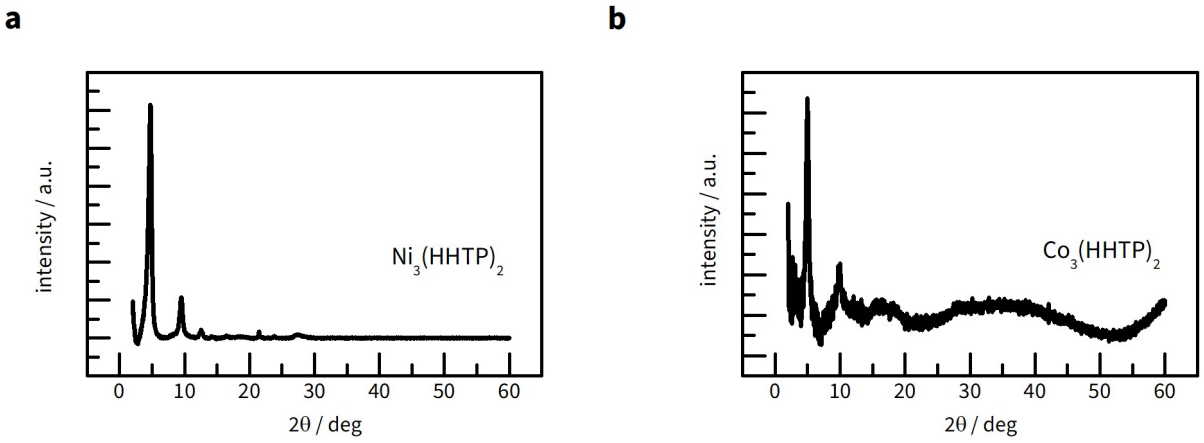

Figure S15. Powder X-ray diffraction (PXRD) patterns obtained for **(a)** $Ni_3(HHTP)_2$ and **(b)** $Co_3(HHTP)_2$.

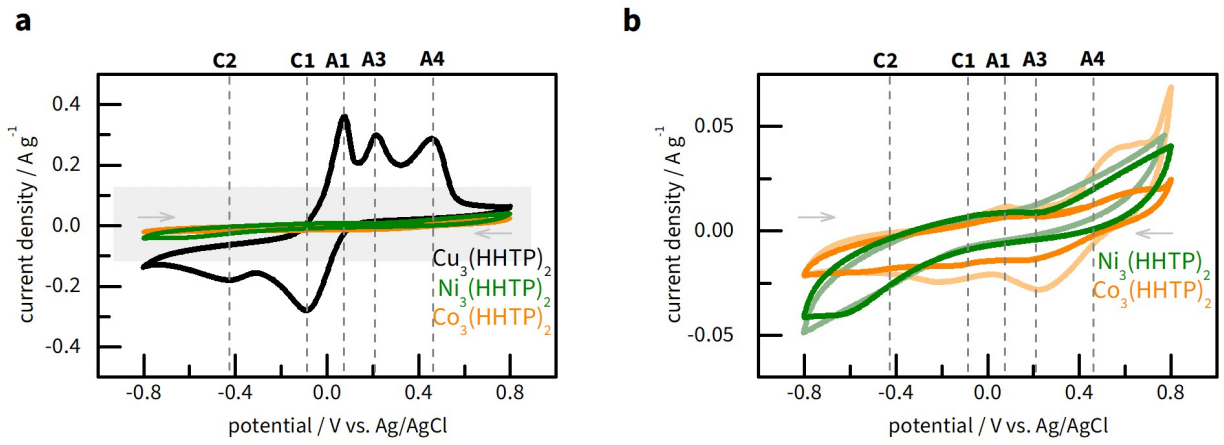

Figure S16. Cyclic voltammetry (CV) curves recorded at a scan rate of 10 mV s^{-1} in 0.1 M $NaClO_4$. (a) CV curves in a CO_2-saturated electrolyte for different electrodes: black – GC-$Cu_3(HHTP)_2$, orange – GC-$Co_3(HHTP)_2$, and green – GC-$Ni_3(HHTP)_2$. (b) CV curves in an Ar-saturated electrolyte for different electrodes: light orange – GC-$Co_3(HHTP)_2$ and light green – GC-$Ni_3(HHTP)_2$; in a CO_2-saturated electrolyte for: dark orange – GC-$Co_3(HHTP)_2$ and dark green – GC-$Ni_3(HHTP)_2$.

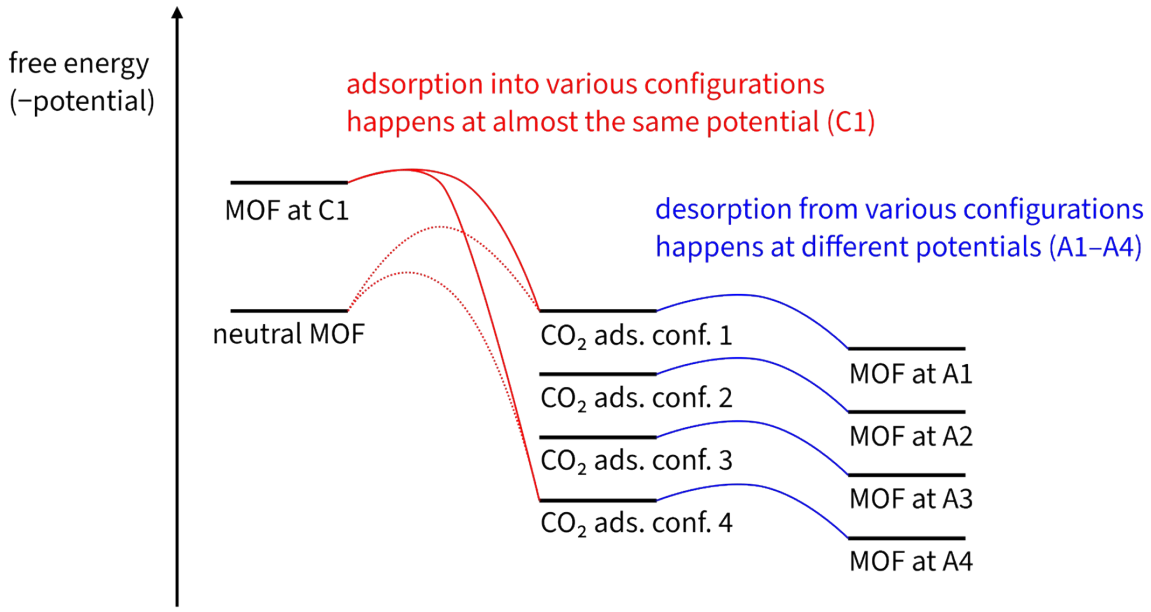

Figure S17. Free energy diagram suggesting that the distinct anodic peaks (A1–A4) are due to desorption from distinct configurations (1–4), in which adsorbed CO_2 has a variable number of neighbouring CO_2 molecules, i.e., different surroundings. We assume that the adsorption at cathodic peak (C1) is governed by the electron transfer from copper to the adsorbing CO_2, which is favoured for forming multiple configurations. The desorption from these configurations requires different potentials.

Density Functional Theory calculations

For all Density Functional Theory (DFT) calculations, open source ASE 3.23.0 and GPAW 24.1.0 packages were used,[19,20] with the RPBE exchange-correlation functional,[21] along with the D4 dispersion correction.[22] The core and valence electrons were described with the projector augmented-wave method. Standard 24.1.0 setups were used for all elements along double-zeta basis sets for obtaining the initial density, and Hubbard U of 10.4 eV for Cu.[23] Grid spacing of ~0.12 Å with a number of grid points divisible by 4 were used. Spin-polarisation was turned on, and the magnetic moment of ±1 was preset on Cu^{2+} ions, with alternating signs for distinct layers. Brillouin-zone sampling was made with 4 k-points in the MOF plane and 2 k-points in perpendicular directions. The named parameters were tested for energy convergence. For all other parameters, default values were taken.

CO_2 adsorption was modelled in finite-difference mode using a solvated jellium model.[24] A constant counter charge of +1*e* per Cu atom was located in the jellium region, 3.5–6.5 Å above the Cu atom. An implicit water layer was put into a cavity between the jellium and MOF to solvate CO_2.[25] In the case of the three-dimensional model of $Cu_3(HHTP)_2$ crystal, only the terminal facet was studied for adsorption due to the limitation of the solvated jellium model, which is currently applicable only to flat electrochemical interfaces. To compare adsorption on the facet and in the pore, simplified two- and one-dimensional slab models were constructed (Fig. S2). Three adsorption sites were considered: above the Cu atom, above the O atom, and above an aromatic ring.

The three-dimensional model of $Cu_3(HHTP)_2$ crystal was created using *in silico* data from the EC-MOF database.[26] Two- and one-dimensional models, mimicking $Cu_3(HHTP)_2$, were created using the optimised parameters of the three-dimensional model (Fig. S2). Optimisation of atomic positions and unit cell parameters of pure MOF models was made in plane wave mode with a cut-off of 600 a.u. and the FrechetCellFilter,[1] until the residual forces of each atom become less than 0.1 eV $Å^{-1}$. Optimisation of atomic positions of MOF models with adsorbed CO_2 was run with the Broyden–Fletcher–Goldfarb–Shanno algorithm until the residual forces on each atom became less than 0.1 eV $Å^{-1}$. Enthalpy, entropy, and free energy values were evaluated at ideal gas and harmonic approximations through a vibrational analysis as implemented in the ASE thermochemistry module.

References

1 T. Shimizu, T. Hirama, H. Hosoda, K. Kitano, M. Inagaki and K. Tejima, *Chem. Eng. Res. Des.*, 1999, 77, 62–68.
2 J. W. Lee, H. Ahn, S. Kim and Y. T. Kang, *J. Clean. Prod.*, 2023, 390, 136141.
3 J. Kumełan, Á. Pérez-Salado Kamps, D. Tuma and G. Maurer, *J. Chem. Thermodyn.*, 2006, 38, 1396–1401.
4 O. Shekhah, Y. Belmabkhout, Z. Chen, V. Guillerm, A. Cairns, K. Adil and M. Eddaoudi, *Nat. Commun.*, 2014, 5, 4228.
5 S. Karka, S. Kodukula, S. V. Nandury and U. Pal, *ACS Omega*, 2019, 4, 16441–16449.
6 Y. Liu, H.-Z. Ye, K. M. Diederichsen, T. Van Voorhis and T. A. Hatton, *Nat. Commun.*, 2020, 11, 2278.
7 J. W. Gittins, C. J. Balhatchet, Y. Chen, C. Liu, D. G. Madden, S. Britto, M. J. Golomb, A. Walsh, D. Fairen-Jimenez, S. E. Dutton and A. C. Forse, *J. Mater. Chem. A*, 2021, 9, 16006–16015.
8 W. Zhao, T. Chen, W. Wang, S. Bi, M. Jiang, K. Y. Zhang, S. Liu, W. Huang and Q. Zhao, *Adv. Mater. Interfaces*, 2021, 8, 2100308.
9 J. W. Gittins, C. J. Balhatchet, S. M. Fairclough and A. C. Forse, *Chem. Sci.*, 2022, 13, 9210–9219.
10 E. M. Miner, L. Wang and M. Dincă, *Chem. Sci.*, 2018, 9, 6286–6291.
11 M. Ko, L. Mendecki, A. M. Eagleton, C. G. Durbin, R. M. Stolz, Z. Meng and K. A. Mirica, *J. Am. Chem. Soc.*, 2020, 142, 11717–11733.
12 S. Gu, Z. Bai, S. Majumder, B. Huang and G. Chen, *J. Power Sources*, 2019, 429, 22–29.
13 K. W. Nam, S. S. Park, R. Dos Reis, V. P. Dravid, H. Kim, C. A. Mirkin and J. F. Stoddart, *Nat. Commun.*, 2019, 10, 4948.
14 K. M. Snook, L. B. Zasada, D. Chehada and D. J. Xiao, *Chem. Sci.*, 2022, 13, 10472–10478.
15 Z. Meng and K. A. Mirica, *Nano Res*.
16 M. Z. Iqbal, M. Shaheen, M. W. Khan, S. Siddique, S. Farid, S. Aftab and S. M. Wabaidur, *Mater. Today Sustain.*, 2023, 22, 100331.
17 T. Abe, G. M. Swain, K. Sashikata and K. Itaya, *J. Electroanal. Chem.*, 1995, 382, 73–83.
18 J.-D. Yi, R. Xie, Z.-L. Xie, G.-L. Chai, T.-F. Liu, R.-P. Chen, Y.-B. Huang and R. Cao, *Angew. Chem. Int. Ed.*, 2020, 59, 23641–23648.
19 A. H. Larsen, J. J. Mortensen, J. Blomqvist, I. E. Castelli, R. Christensen, M. Dulak, J. Friis, M. N. Groves, B. Hammer, C. Hargus, E. D. Hermes, P. C. Jennings, P. B. Jensen, J. Kermode, J. R. Kitchin, E. L. Kolsbjerg, J. Kubal, K. Kaasbjerg, S. Lysgaard, J. B. Maronsson, T. Maxson, T. Olsen, L. Pastewka, A. Peterson, C. Rostgaard, J. Schiøtz, O. Schütt, M. Strange, K. S. Thygesen, T. Vegge, L. Vilhelmsen, M. Walter, Z. Zeng and K. W. Jacobsen, *J. Phys. Condens. Matter*, 2017, 29, 273002.
20 J. J. Mortensen, A. H. Larsen, M. Kuisma, A. V. Ivanov, A. Taghizadeh, A. Peterson, A. Haldar, A. O. Dohn, C. Schäfer, E. Ö. Jónsson, E. D. Hermes, F. A. Nilsson, G. Kastlunger, G. Levi, H. Jónsson, H. Häkkinen, J. Fojt, J. Kangsabanik, J. Sødequist, J. Lehtomäki, J. Heske, J. Enkovaara, K. T. Winther, M. Dulak, M. M. Melander, M. Ovesen, M. Louhivuori, M. Walter, M. Gjerding, O. Lopez-Acevedo, P. Erhart, R. Warmbier, R. Würdemann, S. Kaappa, S. Latini, T. M. Boland, T. Bligaard, T. Skovhus, T. Susi, T. Maxson, T. Rossi, X. Chen, Y. L. A. Schmerwitz, J. Schiøtz, T. Olsen, K. W. Jacobsen and K. S. Thygesen, *J. Chem. Phys.*, 2024, 160, 092503.
21 B. Hammer, L. B. Hansen and J. K. Nørskov, *Phys. Rev. B*, 1999, 59, 7413–7421.
22 E. Caldeweyher, J.-M. Mewes, S. Ehlert and S. Grimme, *Phys Chem Chem Phys*, 2020, 22, 8499–8512.
23 G. W. Mann, K. Lee, M. Cococcioni, B. Smit and J. B. Neaton, *J. Chem. Phys.*, 2016, 144, 174104.
24 G. Kastlunger, P. Lindgren and A. A. Peterson, *J. Phys. Chem. C*, 2018, 122, 12771–12781.
25 A. Held and M. Walter, *J. Chem. Phys.*, 2014, 141, 174108.
26 Z. Zhang, D. S. Valente, Y. Shi, D. K. Limbu, M. R. Momeni and F. A. Shakib, *ACS Appl. Mater. Interfaces*, 2023, 15, 9494–9507.